同行专家业内评价意见书编号：20250856067

附件1

浙江工程师学院（浙江大学工程师学院）
同行专家业内评价意见书

姓名： 唐明军

学号： 22260340

申报工程师职称专业类别（领域）： 材料与化工

浙江工程师学院（浙江大学工程师学院）制

2025年03月21日

填表说明

一、本报告中相关的技术或数据如涉及知识产权保护、军工项目保密等内容，请作脱密处理。

二、请用宋体小四字号撰写本报告，可另行附页或增加页数，A4纸双面打印。

三、表中所涉及的签名都必须用蓝、黑色墨水笔，亲笔签名或签字章，不可以打印代替。

四、同行专家业内评价意见书编号由工程师学院填写，编号规则为：年份4位＋申报工程师职称专业类别(领域)4位+流水号3位，共11位。

一、个人申报

（一）基本情况【围绕《浙江工程师学院（浙江大学工程师学院）工程类专业学位研究生工程师职称评审参考指标》，结合该专业类别(领域)工程师职称评审相关标准，举例说明】

1.对本专业基础理论知识和专业技术知识掌握情况(不少于200字)

在实习实践过程中，我以圆柏精油为研究对象，设计并制造了一系列的同步分离提取系统的装置，利用其提升了圆柏精油的提取效率和精油中γ-
萜品烯的含量，首次实现了精油提取和成分分离富集的同步进行，并对精油进行微乳化处理，增强存储稳定性和抗氧化性能。下面是相关的基础理论知识和专业技术知识：
一、基础理论知识
1. 传质与分离工程
汽-
液平衡（VLE）原理：熟练掌握了混合物在加热过程中气相与液相的组成关系，能够合理调整分离条件，以优化目标产物的纯度和收率。
蒸馏与精馏理论：理解传统的间歇蒸馏，同时运用连续蒸馏、超声辅助蒸馏等技术，提高目标组分的富集效率。
能量核算：通过计算加热系统的功率需求，优化设备参数，提高能量利用率。
2. 物理化学与胶体化学
界面张力控制：理解了表面活性剂的作用，能够利用亲水亲油平衡值（HLB）优化乳化体系，提高微乳液的稳定性。
纳米尺度的胶体分散理论：掌握了微乳液的形成机理，能通过伪三元相图分析不同组分的相行为，优化乳化体系。
热力学稳定性：能够运用吉布斯自由能理论分析微乳液体系的稳定性，并结合实验验证其长期存储性能。
3. 生物化学与抗氧化机制
自由基清除理论：熟练掌握抗氧化剂如何中和自由基，能够使用DPPH、FRAP、超氧阴离子清除等实验方法评估抗氧化能力。
自由基链式反应机制：理解自由基的生成、扩展和终止机制，能够结合实验评估不同化合物的抗氧化效果。
生物分子的保护机制：能够分析抗氧化剂对生物大分子（如脂质、蛋白质）的保护作用，并利用实验数据证明其功能价值。
4. 统计优化与实验设计
响应面优化（RSM）：熟练掌握多变量优化方法，能够基于实验数据建立数学模型，优化关键工艺参数。
数据回归与拟合：能够运用回归分析建立实验数据之间的关系，通过统计分析寻找最优实验条件。
变量交互影响分析：理解实验因素之间的相互作用，能够通过实验设计和统计分析优化实验流程。

二、专业技术知识
1. 精油提取与分离技术
蒸馏提取技术：熟练掌握水蒸气蒸馏、超声辅助蒸馏等方法，优化提取工艺，提高目标成分的富集效率。
设备优化：能够结合全混流反应器、精馏塔等概念，优化传统蒸馏设备，提高产率并降低能耗。
能耗控制与设备参数优化：通过热量衡算、超声功率优化，减少能源浪费，提高提取工艺的

经济性。
2. 微乳液制备与表征
乳化剂筛选与优化：能够选择合适的表面活性剂，并优化HLB值，提高微乳液的稳定性。
粒径分析（DLS）：掌握动态光散射法（DLS），能够分析微乳液的粒径分布，优化乳液体系的均一性。
形态学分析（TEM）：使用透射电子显微镜（TEM）观察微乳液的形貌，评估长期存储的稳定性。
3. 抗氧化实验与评价
自由基清除实验（DPPH、FRAP）：熟练掌握光度法评估抗氧化能力，通过颜色变化定量测定自由基清除能力。
抗氧化剂稳定性分析：能够通过TGA（热重分析）测试抗氧化剂的稳定性，优化其储存条件。
长期存储稳定性评估：能够使用长期存储实验，评估抗氧化剂的降解速率，优化产品货架期。
4. 数据分析与建模
数据处理与统计分析：能够使用Design-Expert、MATLAB等工具进行数据回归分析，提高实验数据的可信度。
实验优化与建模：能够建立数学模型优化工艺参数，提高实验效率并降低成本。
总结
在化学工程、物理化学、生物化学、数据分析等多个领域展现了扎实的基础理论知识，并在精油提取、微乳液制备、抗氧化实验、数据优化等技术方面具有较强的专业技术能力。能够独立开展研究、优化工艺，并推动研究成果的实际应用。

2.工程实践的经历(不少于200字)

工程实践经历——珀莱雅化妆品股份有限公司（2023.12 - 2025.1）
在珀莱雅化妆品股份有限公司的工程实践过程中，我深度参与了化妆品原料的提取、分离、稳定化及其在护肤产品中的应用开发。这次实践不仅让我将理论知识与实际应用紧密结合，还极大地提高了我在精细化工、化妆品配方设计及工程优化方面的专业技能。
1. 精油提取与分离工艺优化
在实践初期，我主要负责天然植物活性成分的提取与分离，特别是精油及多酚类抗氧化物的同步提取。在提取植物活性成分时，我们采用了超声辅助蒸馏和连续化提取技术，以提高精油及其活性成分的提取率。
（1）设备调试与优化
我在实际操作中深入了解了水蒸气蒸馏、超声辅助提取、低温蒸馏等提取技术，并结合传质与热力学原理，对提取设备的核心参数进行优化。通过计算热量衡算和能量利用率，优化加热系统，提高能效，在蒸馏釜外部增加聚氨酯保温层，减少热损失，提高蒸馏效率。同时通过Matlab仿真计算超声场分布，调整振子的排列方式，使空化作用最大化，提高精油释放速率。采用精馏塔的概念重新设计提取釜来分离轻重组分，提高高附加值成分（如γ-萜品烯）的浓度，为后续产品研发提供更纯净的原料。最终，经过多次优化，我们的精油提取率提升了约25%，同时能耗降低了30%，为公司节省了大量生产成本。
2. 精油微乳液的制备与稳定性研究
在护肤品应用方面，我重点参与了精油的微乳化研究，以提高其在水性基质中的分散性和生物利用度。由于精油的水溶性差、挥发性高、易被氧化，我们需要通过乳化技术改善其稳定性，并增强其抗氧化活性。
（1）表面活性剂优化

为了寻找最适合的乳化剂体系，我通过HLB（亲水亲油平衡值）理论，筛选了不同组合的表面活性剂（Tween 60、Span
80）和助表面活性剂（乙醇、丙二醇）。通过绘制伪三元相图，分析不同乳化剂组合的单相区面积，最终确定了最优配方：HLB 值在 9.5-12 时，微乳液形成较稳定，Tween 60
和乙醇的组合具有最佳的乳化效果，提高油相含量至15%时，精油的载量和稳定性最优。
（2）微乳液的物理化学性质分析
为了验证微乳液的稳定性，我使用了动态光散射（DLS）测量粒径分布，并采用透射电子显微镜（TEM）观察其微观结构，当微乳液粒径分布在 5-50 nm 之间，PDI 低于
0.2，说明体系均一稳定，TEM
显示微乳液胶粒呈球形，分布均匀，在长达一年存储后，微乳液依旧透明澄清，无明显分层现象，在此基础上，我们还研究了微乳液的抗氧化性能，通过DPPH自由基清除实验和FRAP实验，验证了其对自由基的清除能力，发现微乳化后，精油的抗氧化能力提升了约
40%，在FRAP
还原能力测试中，微乳液表现优于传统精油溶液，这些研究成果为精油在护肤品中的应用提供了稳定的技术支持。
3. 抗氧化护肤产品开发
基于前期研究成果，我参与了抗氧化护肤产品的配方开发，主要涉及抗氧化精华液、喷雾和水基香水的研发。
（1）抗氧化精华液
结合圆柏精油微乳液和维生素E衍生物，共同提高抗氧化能力，通过pH值调控和电导率分析，确保配方体系的稳定性，采用响应面优化法（RSM），优化乳化体系，提高精华液的肤感和渗透力，最终，研发的抗氧化精华液在体外抗氧化评价实验中表现优异，自由基清除率高达90.54 ± 1.94 μg VC·g^{-1}，达到市场同类高端产品的水准。
（2）水基香水
传统香水以乙醇为溶剂，而我在研究中发现高浓度乙醇对皮肤刺激性较大，精油直接在水中分散稳定性差，香味释放不均
为此，我们采用微乳化技术，成功制备了无酒精水基香水，提高了精油的水溶性，香味释放更持久，同时微乳液体系稳定，喷雾后不留白色沉淀，优化乳化剂后，香水肤感更加清爽，这一创新配方大幅提升了香水的安全性和使用体验。
4. 实践总结
在珀莱雅化妆品股份有限公司的这段实践经历，不仅让我深入理解了化妆品原料的提取、分离、稳定化及应用，更让我在工程优化、实验设计、数据分析、产品开发等方面积累了丰富的经验。

3.在实际工作中综合运用所学知识解决复杂工程问题的案例（不少于1000字）

圆柏精油的高效低成本同步分离提取系统工艺优化及微乳液抗氧化应用
第一章 研究背景与问题分析
1.1 研究背景
珀莱雅在研发天然护肤品时，致力于采用植物活性成分以提升化妆品的功效。圆柏精油因其抗氧化、抗菌、抗炎特性被选为核心成分，但传统水蒸气蒸馏法的精油收率仅为0.05
wt%，远低于文献报道的0.3-0.5
wt%。此外，提取工艺能耗高、精油在水相体系中的分散性差、抗氧化能力不稳定，影响了其在化妆品中的应用。
1.2 研究目标
针对上述问题，本研究的主要目标包括：

1. 优化精油提取工艺，提高收率至0.5 wt% 以上，降低能耗；
2. 提升精油在水性化妆品中的稳定性，减少析出问题；
3. 增强抗氧化能力，提高护肤品功效持续时间。

第二章 解决方案设计与实验方案

2.1 提取工艺优化

为了提高收率并降低能耗，本研究提出了超声辅助结合连续化蒸馏提取系统，并在设备设计和工艺参数优化方面进行了研究。

2.1.1 设备设计

本研究借鉴了全混流反应器和精馏塔的概念，改造传统间歇式蒸馏釜，加入超声模块、加热、搅拌和输送装置，形成同步分离提取系统。核心优化点包括：

- 采用连续化超声辅助蒸馏，提升精油释放效率；
- 优化换热系统，回收蒸馏废液中的热量，降低能耗；
- 同步分离提取精油、多酚、残渣和纯露，提高资源利用率。

2.1.2 关键变量优化

本研究采用Box-Behnken 响应面试验设计，优化以下提取变量：

- 液料比（mL/g）：影响精油溶出效率；
- 超声功率（kW）：影响细胞壁破坏程度；
- 加热功率（kW）：影响蒸馏速率和精油收率。

最终优化出的参数如下：

- 液料比：17.27 mL/g；
- 超声功率：0.56 kW；
- 加热功率：6.39 kW；
- 精油收率：0.532±0.005 wt%，较传统水蒸气蒸馏提升9.9倍。

2.1.3 提取工艺优势

- 生产同样质量的精油时，同步分离提取系统的CO_2排放量仅为水蒸气蒸馏的22.3%；
- 采用5 min 保留时间，圆柏精油的γ-

萜品烯含量达33.75%，高于水下蒸馏（7.08%）和水蒸气蒸馏（4.78%）。

2.2 微乳液体系优化

为了改善精油在水性体系中的稳定性，本研究采用微乳化技术，优化表面活性剂体系，以提高精油的水溶性、存储稳定性和抗氧化性能。

2.2.1 微乳液构建

采用表面活性剂+助乳化剂的方式构建微乳液：

- 表面活性剂：Tween 60 + Span 80
- 助乳化剂：乙醇 + 1,2-己二醇

优化配方：

- 精油含量：2.5 wt%
- 乳化剂/油比：5:1
- 水相 pH：6.5
- 搅拌速度：1200 rpm

优化后的微乳液在60天存储过程中无分层，适用于化妆品体系。

第三章 结果与数据分析

3.1 提取工艺优化结果

优化后的提取工艺在多个方面表现优异：

- 精油收率：0.532 wt%，比传统方法提高9.9倍；
- 能耗降低：77.7%；
- CO_2排放降低：4.5倍；

• γ-萜品烯富集：含量达33.75%。

3.2 微乳液抗氧化性能测试

为了评估微乳液的抗氧化能力，采用DPPH、FRAP、PTIO、超氧自由基清除率等实验方法。

DPPH 自由基清除率：优化后微乳液的清除率为 77.39 ± 1.64 μg VE/g，相比于纯精油的 25.6 ± 1.12 μg VE/g，提高了约 3 倍。

FRAP 还原能力：优化后微乳液的数值为 90.54 ± 1.94 μg VE/g，而纯精油仅为 45.26 ± 1.49 μg VE/g，表明其抗氧化能力提高了 2 倍。

PTIO 自由基清除率：优化后微乳液的清除能力达 297.49 ± 5.55 μg VC/g，远高于纯精油的 129.21 ± 2.78 μg VC/g，说明微乳液体系更能有效清除自由基。

超氧自由基清除率：优化后微乳液的清除率达到 82.7%，明显高于纯精油的 46.3%，表明其在抗氧化方面的稳定性更强。

微乳液存储60天无分层，抗氧化能力下降率 < 5%。

第四章 研究结论

本研究成功优化了圆柏精油提取工艺，并改进了微乳液抗氧化应用：

1. 连续化超声辅助蒸馏工艺将精油收率提高9.9倍，能耗降低77.7%；
2. γ-萜品烯富集，使精油中活性成分含量提升；
3. 微乳化技术优化，提高了精油在化妆品中的稳定性，抗氧化能力提高2-3倍，适用于水基香水和护肤品；
4. 可推广至玫瑰、薰衣草等精油，扩大工业应用。

本研究在提升化妆品抗氧化性能、减少生产成本、提升资源利用率方面具有广阔的市场前景。

（二）取得的业绩（代表作）【限填3项，须提交证明原件（包括发表的论文、出版的著作、专利证书、获奖证书、科技项目立项文件或合同、企业证明等）供核实，并提供复印件一份】

1.
公开成果代表作【论文发表、专利成果、软件著作权、标准规范与行业工法制定、著作编写、科技成果获奖、学位论文等】

成果名称	成果类别 [含论文、授权专利（含发明专利申请）、软件著作权、标准、工法、著作、获奖、学位论文等]	发表时间/授权或申请时间等	刊物名称/专利授权或申请号等	本人排名/总人数	备注
The Elucidation of the Critical Role of HLB value in Microemulsions Formulation	国际期刊	2025年02月13日	ChemNanoMat	1/5	SCI期刊已接收，尚未见刊
一种连续化超声微波辅助提取植物精油的蒸馏装置及方法	发明专利申请	2024年04月10日	申请号：CN202410428810.0	2/3	导师第一
一种采用天然共晶溶剂法从植物中提取的植物黄酮和植物多酚及其方法	发明专利申请	2024年04月10日	申请号：CN202410428811.5	2/3	导师第一

2.其他代表作【主持或参与的课题研究项目、科技成果应用转化推广、企业技术难题解决方案、自主研发设计的产品或样机、技术报告、设计图纸、软课题研究报告、可行性研究报告、规划设计方案、施工或调试报告、工程实验、技术培训教材、推动行业发展中发挥的作用及取得的经济社会效益等】

（三）在校期间课程、专业实践训练及学位论文相关情况	
课程成绩情况	按课程学分核算的平均成绩： 83 分
专业实践训练时间及考核情况(具有三年及以上工作经历的不作要求)	累计时间： 1.4 年（要求1年及以上） 考核成绩： 84 分
本人承诺	
个人声明：本人上述所填资料均为真实有效，如有虚假，愿承担一切责任，特此声明！ 申报人签名：唐明军	

22260340

二、日常表现考核评价及申报材料审核公示结果

日常表现考核评价	非定向生由德育导师考核评价、定向生由所在工作单位考核评价： ☑优秀 ☐良好 ☐合格 ☐不合格 德育导师/定向生所在工作单位分管领导签字（公章）：　　年　月　日
申报材料审核公示	根据评审条件，工程师学院已对申报人员进行材料审核（学位课程成绩、专业实践训练时间及考核、学位论文、代表作等情况），并将符合要求的申报材料在学院网站公示不少于5个工作日，具体公示结果如下： ☐通过 ☐不通过（具体原因：　　） 工程师学院教学管理办公室审核签字（公章）：　　年　月　日

浙 江 大 学 研 究 生 院

攻读硕士学位研究生成绩表

学号：22260340	姓名：唐明军	性别：男	学院：工程师学院	专业：材料与化工	学制：2.5年
毕业时最低应获：24.0学分	已获得：27.0学分			入学年月：2022-09	毕业年月：
学位证书号：		毕业证书号：			授予学位：

学习时间	课程名称	备注	学分	成绩	课程性质	学习时间	课程名称	备注	学分	成绩	课程性质
2022-2023学年秋季学期	数值计算方法		2.0	92	专业选修课	2022-2023学年秋冬学期	研究生论文写作指导		1.0	91	专业选修课
2022-2023学年秋季学期	化学品设计与制造		2.0	88	专业学位课	2022-2023学年春季学期	自然辩证法概论		1.0	73	专业学位课
2022-2023学年秋季学期	工程技术创新前沿		1.5	84	专业学位课	2022-2023学年春夏学期	高阶工程认知实践		3.0	77	专业学位课
2022-2023学年冬季学期	新时代中国特色社会主义理论与实践		2.0	92	专业学位课	2022-2023学年春夏学期	工程伦理		2.0	60	专业学位课
2022-2023学年冬季学期	化工制造安全与环境		2.0	94	专业学位课	2022-2023学年夏季学期	研究生英语基础技能		1.0	70	公共学位课
2022-2023学年秋冬学期	科技创新案例探讨与实战		2.0	90	专业选修课	2022-2023学年春夏学期	化学品制造技术进展		2.0	82	专业学位课
2022-2023学年冬季学期	产业技术发展前沿		1.5	87	专业学位课		硕士生读书报告		2.0	通过	
2022-2023学年秋冬学期	研究生英语		2.0	83	专业学位课						

说明：1.研究生课程按三种方法计分：百分制，两级制（通过、不通过），五级制（优、良、中、及格、不及格）。

2.备注中“*”表示重修课程。

学院成绩校核章：

成绩校核人：张梦依

打印日期：2025-03-20

(19)国家知识产权局

(12)发明专利申请

(10)申请公布号 CN 118240620 A
(43)申请公布日 2024.06.25

(21)申请号 202410428810.0

(22)申请日 2024.04.10

(71)申请人 浙江大学
地址 310058 浙江省杭州市西湖区余杭塘路866号

(72)发明人 凌敏 唐明军 马文静

(74)专利代理机构 杭州求是专利事务所有限公司 33200
专利代理师 万尾甜 韩介梅

(51)Int.Cl.
C11B 9/02(2006.01)

权利要求书2页 说明书5页 附图3页

(54)发明名称

一种连续化超声微波辅助提取植物精油的蒸馏装置及方法

(57)摘要

本发明公开了一种连续化超声微波辅助提取植物精油的蒸馏装置及方法通过进料泵和出料泵实现料液的连续化输送,装置中溶剂使用的水或者含有二氧化碳的气泡水或者氢气的还原水,通过蒸馏罐中的加热装置、超声装置和微波发生装置实现料液中植物组织内精油的提取,通过冷凝装置、油水分离装置实现精油和纯露的分离,本发明实现了精油、纯露的同步分离,解决现有的植物精油蒸馏式提取装置在使用过程中无法连续提取、精油提取率低的问题,适用于颗粒、粉状植物材料中精油的连续提取、具有连续、节水的优点,可显著提高植物精油的提取效率。

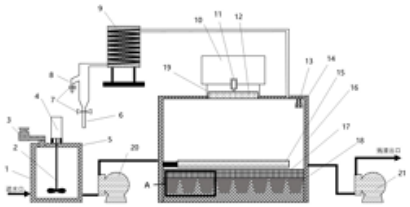

CN 118240620 A

(19)国家知识产权局

(12)发明专利申请

(10)申请公布号 CN 118373861 A
(43)申请公布日 2024.07.23

(21)申请号 202410428811.5

(22)申请日 2024.04.10

(71)申请人 浙江大学
地址 310058 浙江省杭州市西湖区余杭塘路866号

(72)发明人 凌敏 唐明军 马文静

(74)专利代理机构 杭州求是专利事务所有限公司 33200
专利代理师 万尾甜 韩介梅

(51)Int.Cl.
C07G 99/00(2009.01)

权利要求书1页 说明书5页

(54)发明名称

一种采用天然共晶溶剂法从植物中提取的植物黄酮和植物多酚及其方法

(57)摘要

本发明公开了一种采用天然共晶溶剂法从植物中提取植物黄酮和植物多酚的方法，包括以下步骤：将烘干的植物粉碎，向粉碎后的植物中加入天然共晶溶剂NADES浸润，采用水提法加热回流；过滤，将所得滤液离心，取上层清液即为植物黄酮和植物多酚。本发明采用NADES法从植物中提取植物黄酮和植物多酚，该提取方法简单易操作、适用性广、提取效率高、能耗低、对设备条件要求低；对植物的提取工艺研究为植物资源的深层次开发及推广提供科学依据和理论基础。

ChemNanoMat 10.1002/cnma.202400554

WILEY VCH

RESEARCH ARTICLE

The Elucidation of the Critical Role of HLB value in Microemulsions Formulation

Mingjun Tang,[a] Wenjing Ma,[b] Wenqian Sheng,*[b], Wenjun Yan,*[c] Min Ling,*[a][b]

[a] Mr. M. Tang, Prof. M. Ling, Prof. C. Liang
Department Institute of Zhejiang University-Quzhou, Zhejiang University
Institute of New Energy Materials
Zheda Road 99, Quzhou 324000, China
E-mail: minling@zju.edu.cn

[b] Ms. W. Ma, Ms. W. Sheng
College of Chemical and Biological Engineering at Zhejiang University
Department of Chemical and Biological Engineering
Hangzhou 310027, China

[c] Prof. W. Yan,
School of Automation, Hangzhou Dianzi University
Hangzhou 310018, China,

Abstract: Microemulsions are extensively utilized in food, pharmaceuticals, and cosmetics due to their superior solubilizing capacity and protective capabilities. However, a longstanding critical issue with microemulsions is the quantitative relationship between the HLB value and the physicochemical properties. Herein, to quantify the effect of the HLB value on microemulsions, *Juniperus chinensis Rexb.* essential oil (CEO) microemulsions were fabricated. It is certified that HLB values between 8.5 and 11.5 correspond to the smallest biphasic regions, while values between 9.5 and 13.5 correspond to the largest monophasic regions. Besides, the phase evolution from lamellar structures to microemulsions was monitored by the Small-Angle X-ray Scattering (SAXS) patterns. The physicochemical properties of the resulting emulsions, e.g., polydispersity indices (PDI), zeta potential, thermal stability, viscosity, and conductivity, were also investigated. The quantification of the effect of the HLB value on the formation of microemulsions will provide significant quantitative and theoretical guidance to researchers and industry professionals.

1. Introduction

Microemulsions are defined as dispersions composed of water, oil, and surfactants, characterized as isotropic and thermodynamically stable systems with dispersed phase diameters ranging approximately from 1 to 100 nm, typically between 10 to 50 nm.[1] Since Schulman's initial report in the 1940s,[2] microemulsions have been extensively utilized across various domains due to their highly dispersed systems possessing significant interfacial areas. These applications encompass pharmaceutical formulations, cosmetics, food products, oil recovery, and nanomaterial synthesis.[3–7] The HLB (Hydrophilic-Lipophilic Balance) value, a dimensionless number that quantifies the relative hydrophilicity or lipophilicity of a surfactant, is used to describe surfactants' properties. A larger microemulsion formation region typically suggests better stability and versatility. Investigating the quantitative relationship between the HLB values of various surfactants, particularly nonionic surfactants and alcohol co-surfactants, and the areas of biphasic and monophasic regions in microemulsions holds substantial scientific significance.

The research on the quantification of HLB value effect on the formation of microemulsions is barely explored. Only a few related studies have been published. Issa Lo et al. constructed ternary phase diagrams of nonionic surfactant-oil-water systems to investigate the effects of hydrophilic-lipophilic balance (HLB) values and the dielectric constant of the oil phase on emulsion phase behavior. They demonstrated that systems comprising mixtures of two surfactants (e.g., Brij 92 and Brij 96) exhibited significantly higher water solubility across various phases, such as middle and liquid crystalline phases, compared to single surfactants, thus improving emulsion stability and phase distribution.[8] Wang et al. employed varying ratios of Tween 80 and Span 80 to prepare emulsification systems with different HLB values and systematically examined their effects using laser particle analysis, interfacial tension measurements, and stability tests. Their results revealed that an emulsification system with an HLB value of 9.65 produced the smallest average droplet size with the narrowest particle size distribution, alongside a notably reduced interfacial tension, indicating optimal emulsion stability under this HLB condition.[9] Pant et al. evaluated the role of excipients' HLB values in microemulsion systems, systematically analyzing their effects on emulsion formation and stability. They emphasized that surfactants with HLB values between 4-6 are suitable for water-in-oil (W/O) microemulsions, while those with HLB values between 8-18 are ideal for oil-in-water (O/W) systems. Their findings underscored the importance of selecting appropriate HLB values to achieve optimal stability and emulsification properties for different microemulsion types.[10] However, there have been no detailed reports on how the HLB values of surfactants quantitatively affect the size of the single

microemulsion region (W) and biphasic regions in pseudo-ternary phase diagrams, particularly when hydrocarbons are used as the oil phase. Previous studies, such as the work by Reimer et al.[11] investigated the temperature sensitivity and phase behavior of nonionic surfactant systems but did not systematically quantify how HLB values govern the transitions between microemulsion and biphasic regions. This highlights a gap in understanding the quantitative relationship between HLB values and microemulsion formation, which our study aims to address.

This study developed microemulsions of CEO via direct emulsification utilizing various surfactants and co-surfactants. The results demonstrated that HLB values within the range of 8.5 to 11.5 are associated with the smallest biphasic regions, whereas HLB values ranging from 9.5 to 13.5 correspond to the largest monophasic regions. SAXS analysis confirmed that during the preparation of microemulsions, the phase structure evolves from lamellar liquid crystals to bicontinuous phases, eventually transitioning to oil-in-water (O/W) microemulsion structures as the water content increases. Additionally, a comparative analysis of the physicochemical properties of micelles, absent of essential oil, and the resulting microemulsions revealed that the pH of the microemulsions is similar to that of micelles, yet they exhibit larger particle sizes, higher PDI, and lower zeta potential, viscosity, and electrical conductivity. Thermogravimetric Analysis (TGA) suggested the presence of azeotropes involving alcohol-water or alcohol-water-oil systems upon heating. Furthermore, the use of high-boiling medium-chain alcohols was found to enhance the thermal stability of the microemulsions. Finally, in the antioxidant assays, it was observed that the essential oil, after microemulsification, exhibited higher activity against DPPH (1,1-Diphenyl-2-picrylhydrazyl) and PTIO (2-Phenyl-4,4,5,5-tetramethylimidazoline-3-oxide-1-oxyl) free radicals. Quantifying the impact of HLB values on microemulsion formation can provide crucial empirical data and theoretical insights, benefiting both research and industry applications.

2. Experimental section

2.1 Materials

Polysorbate 20 (Tween 20, AR), Polyoxyethylene sorbitan monopalmitate (Tween 40, AR), Polysorbate 80 (Tween 80, AR), Ethyl Alcohol (AR), Hydrogen Peroxide (30%), Ferrous Sulfate Heptahydrate (AR), Salicylic Acid (CP), Ascorbic Acid (VC, AR) were purchased from China National Pharmaceutical Group Chemical Reagent Co., Ltd. (Shanghai, China). Polyoxyethylene (20) sorbitan monostearate (Tween 60, AR) and Maltitol (AR) were supplied by Macklin Reagent Co., Ltd. (Shanghai, China). 1,2-Propanediol (AR), Glycerin (AR), 1,2-Butanediol (AR), 1,3-Butanediol (AR), 1,2-Hexanediol (AR), PTIO (>98%), α-Tocopherol (VE, AR) were purchased from Aladdin Biochemical Technology Co., Ltd. (Shanghai, China). Ethoxylated hydrogenated castor oil (PEG20, AR) and Ethoxylated hydrogenated castor oil (PEG40, AR) were purchased from Shanghai Yien Chemical Technology Co., Ltd. (Shanghai, China). DPPH (>97%) was obtained from TCI Development Co., Ltd. (Shanghai, China). The *Juniperus chinensis Roxb.* essential oil (CEO) components are as follows: D-Limonene (48.9%), p-Cymene (16.6%), Myrcene (12.8%), α-Pinene (12.2%), and β-Pinene (9.4%).

The abbreviations and full names used in this article are shown in the table below:

Table 1 The abbreviations and full names used in this article

Abbreviation	Full name
CEO	*Juniperus chinensis Roxb.* essential oil
SAXS	Small-Angle x-ray scattering
PDI	Polydispersity indices
ATR-FTIR	Attenuated total reflection fourier transform infrared spectroscopy
HLB	Hydrophilic-Lipophilic balance
DPPH	1,1-Diphenyl-2-picrylhydrazyl
PTIO	2-Phenyl-4,4,5,5-tetramethylimidazoline-3-oxide-1-oxyl
TGA	Thermogravimetric analysis
W/O	Water-in-oil
O/W	Oil-in-water
W	Water
D-Area	Dual-Phase Area (This refers to the turbid region in the pseudo-ternary phase diagram of the microemulsion.)
S-Area (W)	Single-Phase Area with High Water Content (This refers to the clear and transparent region in the pseudo-ternary phase diagram of the microemulsion, where the water content exceeds 50% (mass fraction).)
PEG-40	PEG-40 means that ethoxylated hydrogenated castor oil contains a total of 40 oxyethylene groups in its single molecule
PEG-20	PEG-20 means that ethoxylated hydrogenated castor oil contains a total of 20 oxyethylene groups in its single molecule
VE	vitamin E, α- Tocopherol
VC	vitamin C, Ascorbic Acid

The surfactants and co-surfactants used are shown in Table 2.

Table 2 Selected Surfactants and Cosurfactants with Their Corresponding Abbreviations

Surfactant		HLB_S
S-1	Tween 80	15
S-2	Tween 60	14.9
S-3	Tween 40	14.9
S-4	Tween 20	16.7
S-5	Maltitol	10.8
S-6	Ethoxylated hydrogenated castor oil (PEG20)	9.5
S-7	Ethoxylated hydrogenated castor oil (PEG40)	13.5
Co-Surfactant		HLB_{CS}

CS-1	Ethyl Alcohol	7.39
CS-2	1,2-Propanediol	8.94
CS-3	Glycerin	11.09
CS-4	1,2-Butanediol	7.55
CS-5	1,3-Butanediol	7.55
CS-6	1,2-Hexanediol	5.76

2.2 Microemulsion Preparation and Pseudo-Ternary Phase Diagram Construction

The experimental procedures are as follows:

1. Preparation of the Mixtures: The mixed surfactant and co-surfactant (Mix-S) and *Juniperus chinensis Roxb.* essential oil (CEO) were combined in glass vials at mass ratios of 1:9, 2:8, 3:7, 4:6, 5:5, 6:4, 7:3, 8:2, and 9:1.

2.Sealing and Stirring: Each mixture was sealed with rubber stoppers.

3.Water Addition: Water was manually added dropwise to each mixture under continuous stirring at 600 rpm using a magnetic stirrer (WS-2A, 60W) until a transparent emulsion was formed.

4.Observation and Recording of Phase Transition: The transparency of each mixture was observed, and the amount of water added at the point of phase transition (from clear to turbid or from turbid to clear) was recorded.

5.Calculation of Mass Fractions: The mass fractions of the components were calculated based on the recorded data at the phase transition points.

6.Construction of the Pseudo-Ternary Phase Diagram: A pseudo-ternary phase diagram was constructed using the calculated mass fractions to determine the optimal concentrations for the best microemulsion formation. The recorded data is shown in Table 4.

Table 3 The component mass ratios of different Mix-S and their corresponding abbreviations

	Surfactant (ω)	Co-surfactant (ω)	HLB_{Mix}	Micelles	Microemulsion
Mix-S-1	S-2,0.8	CS-1,0.2	13.4	M-1	MCEO-1
Mix-S-2	S-3,0.5	CS-6,0.5	10.3	M-2	MCEO-2
Mix-S-3	S-3,0.75	CS-1,0.25	13	M-3	MCEO-3
Mix-S-4	S-7,0.5	CS-5,0.5	9.7	M-4	MCEO-4
Mix-S-5	S-1,0.8	CS-4,0.2	13.5	M-5	MCEO-5
Mix-S-6	S-2,0.67	CS-5,0.33	13.4	M-6	MCEO-6
Mix-S-7	S-7,0.67	CS-1,0.33	11.5	M-7	MCEO-7
Mix-S-8	S-1,0.8	CS-1,0.2	13.5	M-8	MCEO-8
Mix-S-9	S-4,0.8	CS-2,0.2	15.1	-	-
Mix-S-10	S-4,0.75	CS-1,0.25	14.4	-	-
Mix-S-11	S-6,0.5	CS-6,0.5	7.7	-	-
Mix-S-12	S-6,0.67	CS-1,0.33	9	-	-

The symbol "-" indicates that the mixture of surfactants in this formulation is not suitable for the formulation of oil-in-water microemulsions

With respect to the HLB value of mixed surfactants, it is computed using the following equation:

$$HLB_{Mix-S} = \omega_1 \cdot HLB_S + \omega_2 \cdot HLB_{C-S} \quad (1)$$

where ω_1 and ω_2 are the mass fractions of the surfactant and the co-surfactant, respectively, and HLB_S and HLB_{C-S} are the HLB values of the surfactant and the co-surfactant, respectively. The HLB value of the co-surfactant was calculated using the formula proposed by Griffin:[12]

$$HLB_{C-S} = \frac{20 \cdot M_h}{M} \quad (2)$$

where M_h is the molecular mass of the hydrophilic portion of the molecule, and M is the molecular mass of the entire molecule.

2.3 Phase Transition in Microemulsion Preparation by SAXS

Microemulsion samples at different water mass fractions (0.2, 0.4, 0.6, 0.8, 0.994) were collected along line B2 (Figure 3.F), and their phase structure transitions were tested using SAXS. Line B2 represents a water dilution line under wireless conditions. At this specific ratio (Mix-S-6: Tween 60 (0.67, ω) & 1,3-Butanediol (0.33, ω); with a mass ratio of Mix-S-6 to CEO set at 8: 2), the system remains clear, indicating a single-phase region throughout the water addition process. SAXS profiles were collected using SAXSpace (Xeuss 2.0) at 30W with a Cu Kα radiation source (λ = 1.542 Å). The samples were inserted into 1.5 mm quartz capillaries and measured at 25°C under atmospheric conditions. The sample-to-detector distance was 1.188 m. Data collection was performed using SAXSdrive™.

2.3.1 Guinier's law analysis

Guinier's law states that at low scattering vectors q, the intensity $I(q)$ can be approximated by: [13]

$$I(q) \approx I(0)e^{-\frac{q^2 R_g^2}{3}} \quad (3)$$

where $I(0)$ is the scattering intensity at zero angle (q=0).q is the magnitude of the scattering vector. R_g is the radius of gyration of the particle, which provides a measure of the particle's size. conduct the following analysis.

2.3.2 Overall conformation analysis

The literature indicates that transforming SAXS data into the pair-distance distribution function p(r) aims to study the geometric characteristics of particles in real space more intuitively. p(r) reflects the frequency distribution of vector distances within particles, allowing the determination of the maximum dimension R_{max} and morphological features. Specifically, $p(r)$ is obtained by applying a Fourier transform to the measured scattering intensity $I(q)$: [14]

$$p(r) = \frac{\int_0^{\infty} I(q) \cdot q \cdot r \cdot \sin(qr) dq}{2\pi^2} \quad (4)$$

For particles with uniform electron density, $p(r)$ represents the frequency of vector lengths r connecting small volume elements within the particle, with a maximum dimension R_{max}. Furthermore, the squared radius of gyration R_g^2, which elucidates the particle's spatial extent and morphology, is derived from the normalized second moment of $p(r)$: [14]

$$R_g^2 = \frac{\int_0^{R_{max}} p(r) \cdot r^2 dr}{2 \int_0^{R_{max}} p(r) dr} \quad (5)$$

Compared to directly using scattering data, p(r) provides a clearer understanding of particle shape changes and their behavior under different physical conditions, facilitating deeper insights into the spatial structure and phase characteristics of the system.

WILEY VCH

RESEARCH ARTICLE

2.3.3 Porod law analysis

The Porod law elucidates the relationship between surface roughness and morphology of disordered materials at large scattering angles and the corresponding scattering intensity. This can be expressed by the following equation: [15]

$$I(q) \propto q^{-4} \quad (6)$$

By performing a fit of q^2~q^4·I(q), the subsequent equation can be obtained: [16]

$$\lim_{q\to\infty} \ln[q^4 \cdot I(q)] = \ln K + b \cdot q^2 \quad (7)$$

For an ideal two-phase system characterized by sharp boundaries, the parameter b =0. However, in the presence of slight thermal density fluctuations or electron density variations, b >0, with its magnitude qualitatively indicating the size of the fluctuation region. In quasi-two-phase systems with diffuse phase boundaries or an interfacial transition zone between the phases, scattering intensity diminishes, particularly at higher angles, b<0, as depicted in Figure 1.

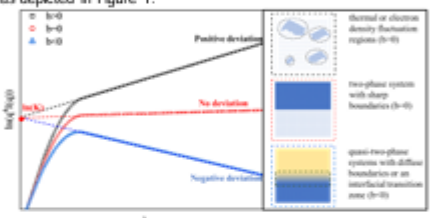

Figure 1 Porod Curves Under Different Deviations and Their Corresponding System State Diagrams

2.3.4 Fractal analysis

The analysis of the scattering effects from complex, disordered materials is significantly simplified when fractal geometry is employed to describe their structure. The SAXS intensity from fractal objects follows a straightforward power-law form by BALE:[17]

$$I(q) = B + Cq^{-\alpha} \quad (8)$$

where *B*, *C* and -*α* are constants. *B* accounts for background scattering or atomic-scale density fluctuations. *C* reflects the scattering contrast and overall material properties. -*α* represents the scattering behavior of the fractal object and is directly related to the fractal dimension D_f by $\alpha = D - 3$, where *D* is the Hausdorff dimension. By fitting -*α*, the fractal dimension can be deduced, providing insights into the surface roughness and structural complexity of the material.

This approach is adopted because fractal geometry reduces complex disordered systems to a few parameters, such as D_f, which quantitatively describe their structure. The fractal dimension indicates whether the material forms three-dimensional networks ($D_f \approx 3$), layered structures ($D_f \approx 2$), linear structures ($D_f \approx 1$), or sparse systems ($D_f < 1$). Furthermore, comparing experimentally derived D_f with theoretical simulations offers deeper insights into phase transitions and structural evolution in such systems.

2.4 Microemulsion characterisation

Different formulations adhering to the specific mass ratio derived from the single-phase region of the phase diagram (CEO: Mix-S: Water = 1:4:15) were prepared to produce essential oil microemulsions and micelles without essential oil (with water substituting for the essential oil). The physicochemical properties of the microemulsions were characterized using the following methods.

2.4.1 pH

The pH of the emulsion was measured using a FiveEasy Plus potentiometer (Mettler Toledo, USA) at 25°C.

2.4.2 Viscosity

The viscosity of the microemulsion was measured using a MARS 60 rheometer (HAAKE, Germany) at 25°C with a shear rate of 0.02 s^{-1}.

2.4.3 Size and polydispersityindices (PDI)

PDI is a measure of the width of size distribution in a dispersed system, such as colloids, nanoparticles, polymers, or molecules. It is an important parameter for describing the uniformity and size distribution range of a sample. After equilibration for a period of 24 h, the microemulsions were diluted with deionized water to the instrument sensitivity range to measure the mean particle diameter using a Zetasizer Nano ZS (Malvern Instruments, UK). The measurements were performed at a 173° scattering angle.

2.4.4 Zeta-potential measurement and conductivity

The zeta-potential values and conductivity of the emulsions were measured at room temperature using the Zetasizer Nano ZS (Malvern Instruments, UK) and the DDB-303A conductivity meter (Shanghai Electronics Science Instrument Co., Ltd., China) at 25°C. Each sample was equilibrated for at least 1.5 h before testing. This equilibration time was essential for keeping samples clear and ensuring the phase diagram remained unchanged.

2.4.5 Attenuated Total Reflection Fourier Transform Infrared Spectroscopy (ATR-FTIR)

The ATR-FTIR spectra of water, *J. chinensis Roxb.* essential oil (CEO), micelles (M), microemulsion of *J. chinensis Roxb.* essential oil (MCEO), surfactants and co-surfactants were obtained using a Nicolet iS50 FTIR spectrometer (Thermo Fisher, USA) equipped with an Attenuated Total Reflection (ATR) module. Each static spectrum was the average of 32 scans in the range of 4000 to 400 cm^{-1} with a spectral resolution of 4 cm^{-1}.

2.4.6 Thermogravimetric Analysis (TGA)

TGA analyses of *J. chinensis Roxb.* essential oil (CEO), micelles (M), microemulsion of *J. chinensis Roxb.* essential oil (MCEO), surfactants and co-surfactants were conducted using a Pyris 1 TGA (Perkin-Elmer, USA) with a heating rate of 5 °C·min^{-1} under nitrogen and synthetic air purge gases, each with a flow rate of 10 mL·min^{-1}. The analyses were performed in an α-alumina crucible over a temperature range of 30–250°C.

2.5 Free radical trapping ability

WILEY-VCH

2.5.1 DPPH radical scavenging assay

The DPPH radical scavenging activity assay is a common in vitro method used to evaluate the total radical scavenging capacity of antioxidants in alcohol-soluble environments. This method was applied to assess the total radical scavenging capacity of the prepared microemulsions in such environments. The free radical scavenging activity of *J. chinensis Roxb.* essential oil (CEO), micelles (M) and microemulsion of *J. chinensis Roxb.* essential oil (MCEO) were assessed using the DPPH assay. The method was slightly modified based on the procedure described by Asres et al., [18] and the specific steps are as follows: 2 mL of 0.1 mM DPPH solution was added to 0.5 mL of MCEO, and the mixture was left in the dark for 30 minutes. Absorbance was measured at 517 nm. Results were expressed in vitamin E equivalents based on the calibration curve (0, 10, 20, 40, 80 μg·mL^{-1}). The inhibition percentage was calculated with the formula:

$$\text{Inhibition}(\%) = \frac{AB\text{-}AA}{AB} \times 100\% \quad (9)$$

where *AB* is the absorbance of the blank, and *AA* is the absorbance of the sample.

2.5.2 PTIO radical scavenging assay

Although the DPPH radical scavenging assay is a widely used in vitro method for antioxidant evaluation, it is not sufficiently accurate or comprehensive for assessing the radical scavenging capacity of microemulsions alone. This is because the DPPH assay requires an alcohol-soluble environment, whereas MCEO has an O/W structure and is water-soluble. To achieve a more accurate evaluation of the total radical scavenging capacity in a water-soluble environment, the water-soluble PTIO radical scavenging assay was adopted, based on the method described by Li et al.,[19] with slight modifications: 2 ml PTIO test solution(0.6 mM) was added to 0.50 mL of MCEO. The mixture was swirled for 6 h in the water of 37°C, Absorbance of the samples was measured at 586 nm. Results were expressed in vitamin C equivalents based on the calibration curve (0, 50, 100, 250 and 500 μg·mL^{-1}). The percentage reduction or inhibition of PTIO radical scavenging activity was identical to that used for DPPH.

2.5.3 Hydroxyl radical scavenging assay

DPPH and PTIO radicals are commonly used for evaluating radical scavenging capacity but cannot assess the scavenging ability of antioxidants against specific radicals such as hydroxyl, superoxide, or nitric oxide radicals. Hydroxyl radicals were selected as the target due to their high reactivity and prevalence in the human body. Based on the method of Li et al., [20] with slight modifications, the specific steps are as follows: 1 mL MCEO was mixed with 0.5 mL FeSO4(6 mM), 1 mL salicylic acid (8 mM), and 0.5 mL H_2O_2 (24 mM). After the mixture is evenly mixed and stand for 1 h in the dark, the absorbance value is measured at 510 nm by UV spectrophotometer. Results were expressed in vitamin C equivalents based on the calibration curve (0, 50, 100, 250, 500 and 1000 μg·mL^{-1}). The percentage reduction or inhibition of the hydroxyl radical scavenging activity was identical to that used for DPPH.

2.6 Statistical analysis

All measurements were performed in triplicates and data were reported as calculated means and standard deviations.

3. Results and Discussion

3.1 Effect of Mix-S type on area of MCEO phase diagram

To achieve optimal emulsification, short-chain alcohols are used as co-surfactants with selected surfactants to form mixed surfactants (Mix-S). The pseudo-ternary phase diagrams of the CEO with several Mix-S were shown in Figure 3.A to Figure 3.L. Previous extensive research has elucidated that the phase behaviour of emulsion systems is a function of both composition and temperature.[21] The formation of microemulsions is intrinsically linked to the interfacial tension of the system. Microemulsions are generated only when the augmentation in interfacial free energy is sufficiently minimal, thereby allowing the entropic driving force of the dispersion process to predominate.[22] The spontaneous curvature of the phase interface in microemulsions can be described by the dimensionless packing parameter *p*:[23]

$$p = \frac{vh}{ah \cdot L} \quad (10)$$

where vh represents the hydrophobic volume of all surfactants and co-surfactants, ah is the area required by all amphiphilic molecules at the interface, and L indicates the length of the hydrophobic segment. The spontaneous curvature of the interface can be effectively modulated by the introduction of co-surfactants. Although the contribution of co-surfactant molecules to the interfacial area is negligible, they significantly augment the hydrophobic volume, thereby diminishing the spontaneous curvature and consequently enhancing the packing parameter (Figure 2).[24] Macroscopically, correlating the optimal compositions of various ratios between surfactants and co-surfactants with their HLB values enables the rapid identification of the most suitable formulations of surfactants and co-surfactants.

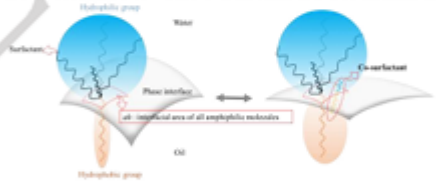

Figure 2 Schematic diagram illustrating how co-surfactant molecules increase hydrophobic volume, reduce spontaneous curvature, and enhance the packing parameter.

The proportion of D-Area and S-Area (W) (Table 1) in microemulsion systems with HLB values of different Mix-S was shown in Figure 3.M, which revealed that microemulsions formed by mixed surfactants with HLB values within the range of 8.5-11.5 showed small D-Area, while those within the HLB range of 9.5-13.5 displayed expanded S-Area (W). This result differs from Ponphaiboon et al.'s finding that the optimal stability of ostrich oil emulsions was achieved at an HLB value of 5.5. [25,26] The difference is due to the fatty acid composition of ostrich oil, compared to the monoterpenes in essential oils, and the absence of co-surfactants in ostrich oil emulsions, resulting in different surfactant systems. The phenomenon could be attributed to the intercalation of co-surfactant molecules among surfactant molecules, thereby reducing interfacial tension. Inadequate co-surfactant molecules failed to effectively reduce interfacial tension,

WILEY VCH

RESEARCH ARTICLE

whereas excess co-surfactant molecules might cause spontaneous curvature of droplets from concave to convex, resulting in droplet instability, coalescence, and demulsification, thereby enlarging the biphasic non-microemulsion domain.[21] A comparison of the S-Area (W) between A and F, G and H, K and L revealed that co-surfactants with intermediate chain lengths (such as 1,2-butanediol and 1,2-hexanediol) exhibited superior co-solvency properties at suitable ratios. Similar to the findings of Gradzielski et al., [24] where co-surfactants such as 1-hexanol were shown to significantly enhance the solubilization capacity of the system by altering interfacial tension and molecular arrangement. The anomalies observed in D and G could be attributed to ethoxylated hydrogenated castor oil (PEG40) having larger hydrophilic groups, thus facilitating the easy ingress of smaller ethanol molecules into the shell layer among surfactant molecules during droplet formation, thereby reducing interfacial tension.

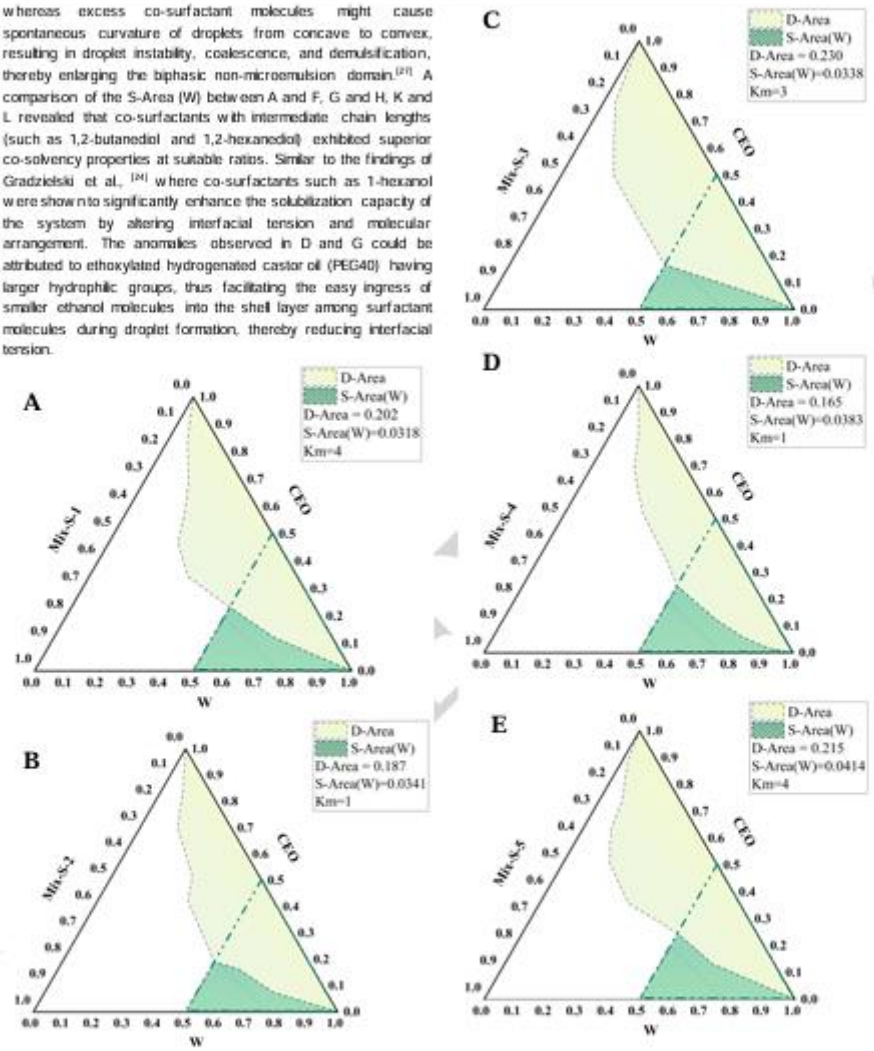

WILEY VCH

RESEARCH ARTICLE

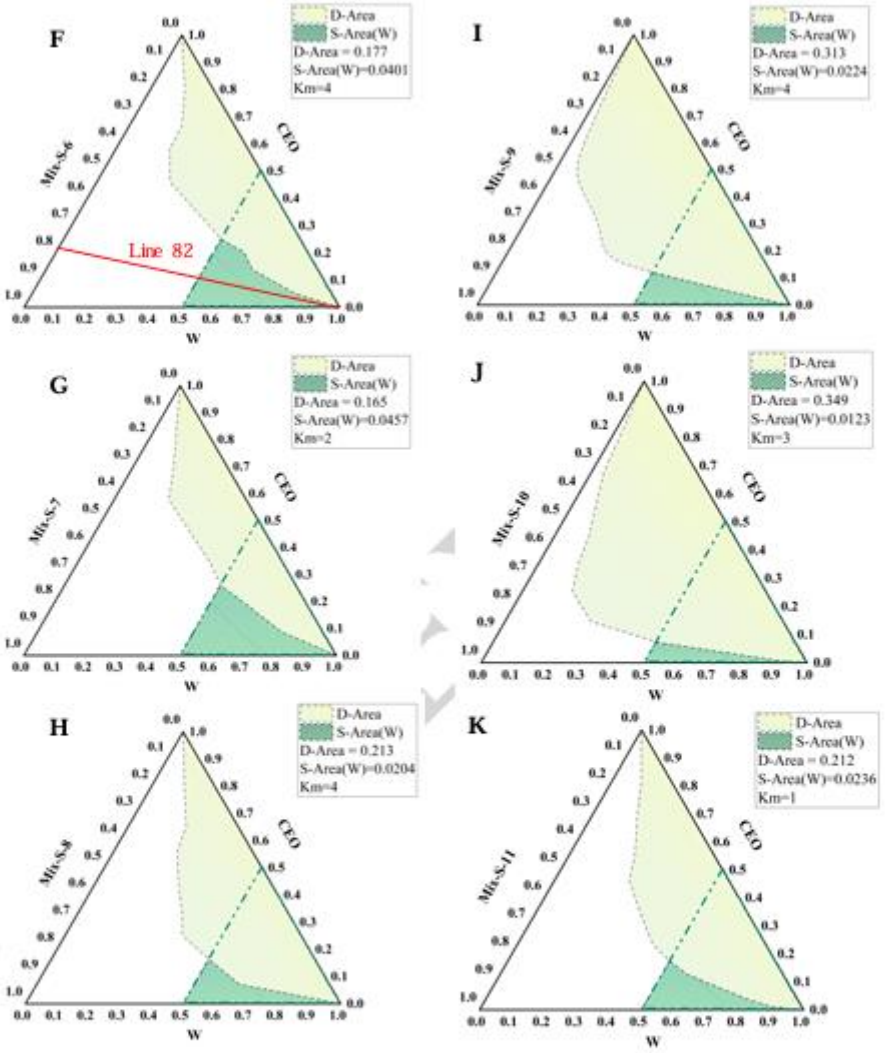

10.1002/cnma.202400554

WILEY VCH

RESEARCH ARTICLE

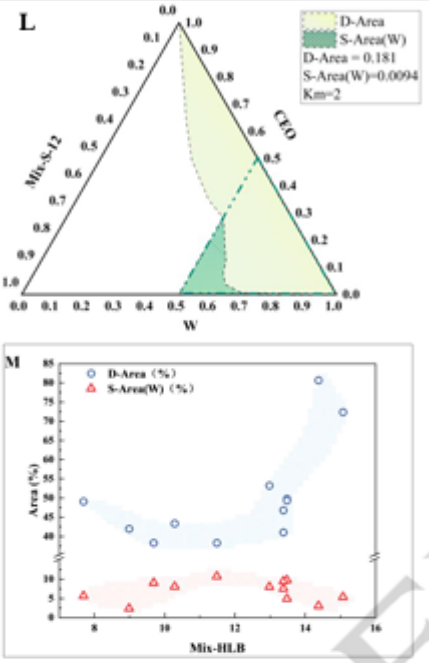

Figure 3 Pseudo-ternary phase diagrams with different Mix-S and the relationship between the HLB values of Mix-S and the D-Area and S-Area (W) (A: Pseudo-ternary phase diagram of CEO with Mix-S-1 (Tween 60 (0.8, ω) & Ethyl Alcohol (0.2, ω)); B: Pseudo-ternary phase diagram of CEO with Mix-S-2 (Tween 40 (0.5, ω) & 1,2-Hexanediol (0.5, ω)); C: Pseudo-ternary phase diagram of CEO with Mix-S-3 (Tween 40 (0.75, ω) & Ethyl Alcohol (0.25, ω)); D: Pseudo-ternary phase diagram of CEO with Mix-S-4 (Ethoxylated hydrogenated castor oil (PEG40) (0.5, ω) & 1,2-Hexanediol (0.5, ω)); E: Pseudo-ternary phase diagram of CEO with Mix-S-5 (Tween 80 (0.8, ω) & 1,2-Butanediol (0.2, ω)); F: Pseudo-ternary phase diagram of CEO with Mix-S-6 (Tween 60 (0.67, ω) & 1,3-Butanediol (0.33, ω)); G: Pseudo-ternary phase diagram of CEO with Mix-S-7 (Ethoxylated hydrogenated castor oil (PEG40) (0.67, ω) & 1,2-Butanediol (0.33, ω)); H: Pseudo-ternary phase diagram of CEO with Mix-S-8 (Tween 80 (0.8, ω) & Ethyl Alcohol (0.2, ω)); I: Pseudo-ternary phase diagram of CEO with Mix-S-9 (Tween 20 (0.8, ω) & 1,2-Propanediol (0.2, ω)); J: Pseudo-ternary phase diagram of CEO with Mix-S-10 (Tween 20 (0.75, ω) & Ethyl Alcohol (0.25, ω)); K: Pseudo-ternary phase diagram of CEO with Mix-S-11 (Ethoxylated hydrogenated castor oil (PEG20) (0.5, ω) & 1,2-Hexanediol (0.5, ω)); L: Pseudo-ternary phase diagram of CEO with Mix-S-12 (Ethoxylated hydrogenated castor oil (PEG20) (0.67, ω) & Ethyl Alcohol (0.33, ω)); M: The proportion of D-Area and S-Area (W) in microemulsion systems with HLB values of different Mix-S.)

Table 4 Table of water fraction (mass fraction) data for different systems

	Water fraction											
CEO:Mix-S	Mix-S-1	Mix-S-2	Mix-S-3	Mix-S-4	Mix-S-5	Mix-S-6	Mix-S-7	Mix-S-8	Mix-S-9	Mix-S-10	Mix-S-11	Mix-S-12
1:9	-	-	-	-	-	-	-	-	-	0.91	0.90	0.63
2:8	-	-	-	0.91	-	-	-	0.64	0.94	0.26	0.80	0.60
3:7	-	0.75	-	0.81	-	0.84	-	0.50	0.30	0.15	0.58	0.59
4:6	0.69	0.59	0.91	0.69	0.67	0.65	0.78	0.37	0.25	0.12	0.42	0.56
5:5	0.31	0.40	0.33	0.50	0.29	0.50	0.60	0.33	0.07	0.11	0.33	0.52
6:4	0.22	0.30	0.17	0.41	0.15	0.23	0.42	0.26	0.04	0.07	0.23	0.42
7:3	0.19	0.26	0.11	0.25	0.09	0.17	0.17	0.20	0.00	0.04	0.20	0.29
8:2	0.14	0.12	0.04	0.14	0.07	0.17	0.13	0.18	0.00	0.00	0.14	0.21
9:1	0.06	0.07	0.00	0.09	0.02	0.11	0.07	0.10	0.00	0.00	0.09	-

"-" indicates that no phase transition point was observed during the water addition process.

WILEY VCH

RESEARCH ARTICLE

3.2 Phase Transition in Microemulsion Preparation

At 25°C, SAXS diffraction was performed on the mixture along dilution line 82 of the pseudo-ternary phase diagram (Figure 3.F). The results were depicted in Figure 4.

3.2.1 Guinier's law analysis

As illustrated in Figure 4.A, at low water content (0.2, ω), the SAXS data revealed a sharp, strong peak at q1 = 0.0729 $Å^{-1}$, alongside a noticeable liquid crystal diffraction peak at q2 = 0.1460 $Å^{-1}$, with a ratio q1: q2 = 1:2. This ratio is characteristic of a lamellar liquid crystalline phase. Referring to the processing method used by Liu et al. [28] By combining the Bragg's law $2d\sin\theta=n\lambda$ and the relationship between the scattering vector q and the angle θ, $q=4\pi\sin\theta/\lambda$, the relationship between the q-value and the interplanar spacing d is obtained as $q=2n\pi/d$, where θ is the incident angle, n is the diffraction order, and λ is the X-ray wavelength, the layer spacing was determined to be 86.1 Å. As the water content increased to 0.4 (ω), a high-intensity sharp peak was observed in the low q-value region at q1 = 0.0587 $Å^{-1}$. Concurrently, diffraction peaks corresponding to the lamellar liquid crystal phase were observed at q2 = 0.0664 $Å^{-1}$ and q3 = 0.1336 $Å^{-1}$, indicating an initial lamellar spacing of 95.2 Å. This suggests that the increase in water content leads to an expansion of the lamellar spacing. With a further increase in water content to 0.6, the diffraction peaks of the lamellar liquid crystal phase disappeared, and a strong, broad peak appeared at q = 0.051 $Å^{-1}$, indicating the presence of larger structures in the system, possibly indicating the formation of a bicontinuous phase. These transitions are similar to the results previously reported by Kogan et al. [29] Additionally, a low-intensity broad peak was observed at q = 0.1354 $Å^{-1}$, indicative of an O/W structure. [30] As the water content continued to increase, the high-intensity diffraction peaks across the entire q-value range disappeared, while the low-intensity weak diffraction peak shifted towards lower q-values. [29]

3.2.2 Overall conformation analysis

Morphological information about the colloidal particles, including their maximum dimensions, can be obtained from the configuration of the pair distance distribution function $p(r)$, as illustrated in Figure 4.B. At lower water contents (from 0.2 to 0.4, ω), the maximum real-space dimension expanded from 41.9 Å to 49.7 Å, corresponding to changes in the interlayer spacing of the lamellar liquid crystal phase. As the water content increase to 0.6, the symmetry of $p(r)$ further deteriorated, with the maximum real-space dimension extending to 57.5 Å. This indicates that the system transitioned from a lamellar, ordered liquid crystal structure to a larger, more disordered bicontinuous phase. With further increases in water content, the system's maximum real-space dimension gradually decreased and the symmetry of $p(r)$ improved.[14] At a water content of 0.994, $p(r)$ exhibited high symmetry, reflecting the geometric characteristics of spherical particles, with a maximum real-space dimension of 19.7 Å.

3.2.3 Porod's law analysis

The correlation plot obtained from Porod's law was depicted in Figure 4.C. All systems displayed positive deviations, suggesting additional scattering induced by subtle electron density fluctuations within the system.[31] The scale of regions with inhomogeneous electron density could be characterized by b, and a decrease in water content reduced the extent of these regions.

3.2.4 Fractal analysis

The fitting results for the fractal dimension of the system at various water contents were illustrated in Figure 4.D. The scatterers exhibited mass fractals under varying water contents. As the water content increased, the fractal dimension of the system rose from 2.08 (at 0.2 ω) to 2.70 (at 0.4 ω), indicating that the complexity of the lamellar liquid crystal structures increased with the rising water content, and the density variations became more pronounced with size changes. This observation was also validated by the spacing between the lamellar structures. Further increasing the water content led to a gradual decrease in the fractal dimension to 0.42 (at 0.994 ω), suggesting that the system's structure became increasingly simple and compact. Which referring to the example results of lignite samples mentioned in the study by Bale et al. [31]

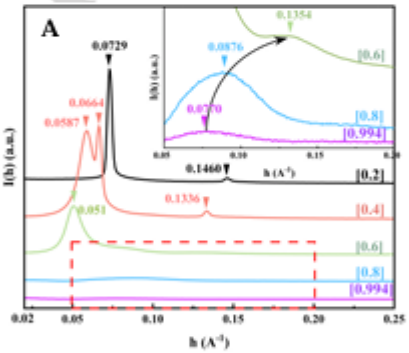

10.1002/cnma.202400554

WILEY VCH

RESEARCH ARTICLE

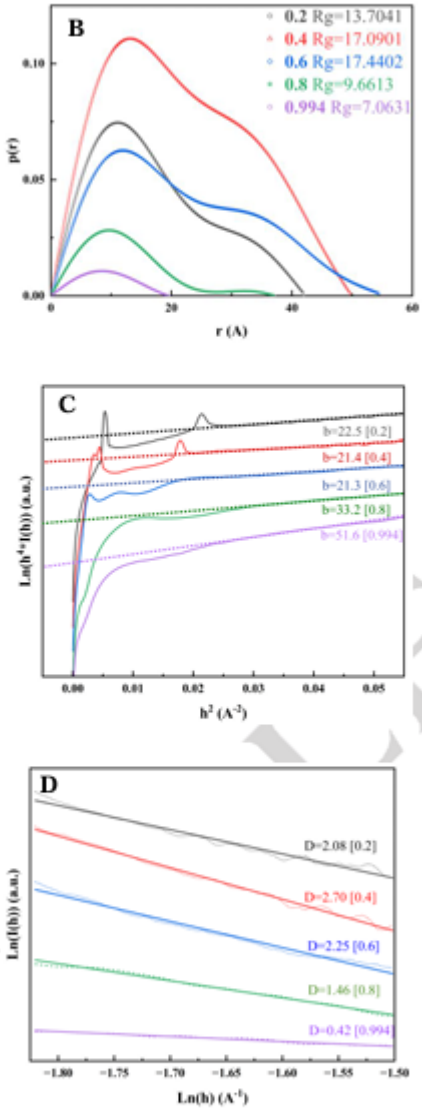

Figure 4 SAXS results of microemulsions with different water contents along line B2. A) q vs. I(q), the inset in the upper right corner shows an enlargement of the red dashed box. B) distance distribution function p(r) obtained from Fourier transform, C) fitting results according to Porod's law, D) fractal dimension obtained from fitting SAXS data

In conclusion, at 0.2 water content, the microemulsion was entirely composed of a high-viscosity lamellar liquid crystalline phase. As the water content increased, the interlayer spacing of the lamellar structure expanded, resulting in increased structural complexity and density fluctuations, and a transition to a bicontinuous phase with interspersed water and oil. The lamellar phase disappeared and was replaced by a large-scale, disordered bicontinuous structure when the water content increased to 0.6. With further increases in water content, the oil was progressively separated and isolated by the water, forming ellipsoidal colloidal particles that became increasingly ordered. At 0.994 water content, the ellipsoidal particles fully transformed into highly symmetrical spherical structures (Figure 5).

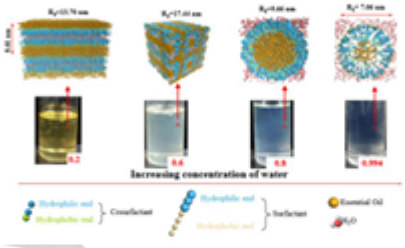

Figure 5 Phase structure evolution of microemulsions with decreasing water content

3.3 Physicochemical properties of microemulsions

The results of microemulsion characterization, including pH, particle size, PDI, zeta potential, conductivity, and viscosity, are shown in Figure 6. These results are discussed separately as follows.

3.3.1 Size, pH, viscosity, PDI, zeta-potential measurement and Conductivity

The pH values of micelles and microemulsions after essential oil incorporation exhibited negligible variation. The conspicuously low pH values of micelles and essential oil microemulsions prepared with Mix-S-1 and Mix-S-6 were may be related to the smaller particle size of the microemulsions prepared with Tween 60, which results in a higher specific surface area, providing more space for the adsorption of hydroxide and hydrogen ions, leading to a lower pH value. The particle sizes of micelles containing Mix-S-1 and Mix-S-6 markedly exceeded the microemulsion range, manifesting visually as milky turbid liquids, a phenomenon not observed following the addition of essential oils. The selection of microemulsion ratios was based on the phase diagram, whereas oil-free micelles (empty microemulsion shells) exhibited demulsification at ambient temperature, likely due to Tween 60 solidification at reduced temperatures in the absence of oil molecules. Other micelles exhibited significant expansion upon the addition of essential oil, resulting in increased particle sizes. Among them, the M-2 micelles experienced the least expansion,

with their diameter increasing from 9.9 nm to 16.7 nm. In contrast, the M-5 micelles demonstrated the greatest expansion, with their diameter increasing from 8.3 nm to 34.9 nm. In other groups, the incorporation of essential oils precipitated micelle diameter expansion and increased PDI, while the absolute zeta potential values were diminished compared to the corresponding micelles. The absolute zeta potential values for these microemulsions and micelles ranged from 0.1 to 0.8, potentially correlated with the selected proportions being close to the microemulsion phase diagram boundary. Conductivity demonstrated a positive correlation with absolute zeta potential values.[32] The shear viscosities of all microemulsions were lower than that of the corresponding micelles, possibly due to enhanced interparticle interactions resulting from the smaller diameters of the micelles.

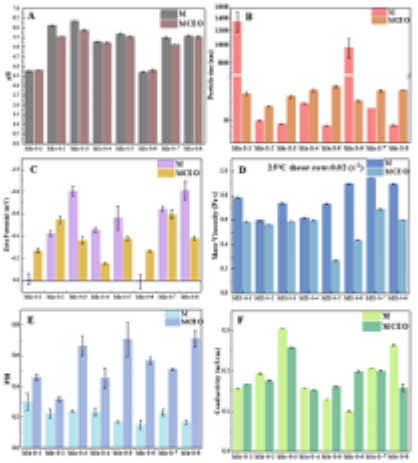

Figure 6 Summary of A) pH, B) particle size, C) zeta potential, D) viscosity, E) PDI, and F) conductivity results for microemulsions prepared with different Mix-S (W/Mix-S = 0.2:0.8 from M-1 to M-8, O/W/Mix-S = 0.05:0.2:0.75 from MCEO-1 to MCEO-8) (Composition of the Mix-S-1 : Tween 60 (0.8, uL) & Ethyl Alcohol(0.2, uL); Mix-S-2 : Tween 40 (0.5, uL) & 1,2-Hexanediol (0.5, uL); Mix-S-3 : Tween 40 (0.75, uL) & Ethyl Alcohol (0.25, uL); Mix-S-4 : Ethoxylated hydrogenated castor oil (PEG40) (0.5, uL) & 1,2-Hexanediol (0.5, uL); Mix-S-5 : Tween 80 (0.8, uL) & 1,2-Butanediol (0.2, uL); Mix-S-6 : Tween 60 (0.67, uL) & 1,3-Butanediol (0.33, uL); Mix-S-7 : Ethoxylated hydrogenated castor oil (PEG40) (0.67, uL) & 1,2-Butanediol (0.33, uL); Mix-S-8 : Tween 80 (0.8, uL) & Ethyl Alcohol (0.2, uL).)

3.3.2 ATR-FTIR of various micelles and microemulsions

The attenuated total reflectance Fourier transform infrared (ATR-FTIR) spectra of various micelles and microemulsions ranging from 400 cm^{-1} to 4000 cm^{-1} are depicted in Figure 7. The infrared spectra of micelles (M-1 to M-8) exhibited a high degree of congruence with their corresponding microemulsions (MCEO-1 to MCEO-8). This indicated that the colloidal particles in the microemulsions possessed a surface state analogous to the micelles in the aqueous solution, suggesting that CEO had infiltrated the interior of the colloidal particles, thus forming an O/W structure. In particular, the broad peak in region Ⅰ and the peak in region Ⅲ were attributed to the O-H stretching vibration and H-O-H bending vibration of water molecules, respectively. The peak in region Ⅱ was primarily caused by the stretching vibrations of the $-CH_3$ and $-CH_2$ groups in the surfactant and co-surfactant. The detailed structure within region Ⅳ was shown in the upper right corner of each subfigure in Figure 7. The CO stretching vibration peak of primary alcohol at 1050 cm^{-1} (point a) indicates the presence of different co-surfactant molecules (short-chain alcohols) on the surface of the microemulsions or micelles, thereby confirming the presence of these molecules.[24] Comparing A, C, G and H with B, D, E and F in Figure 7, the C-O stretching vibration peak in microemulsions or micelles with ethanol as a co-surfactant was more pronounced than with other co-surfactants. This heightened intensity is likely due to ethanol's smaller molecular weight, which results in a higher molar concentration at an equivalent mass fraction.

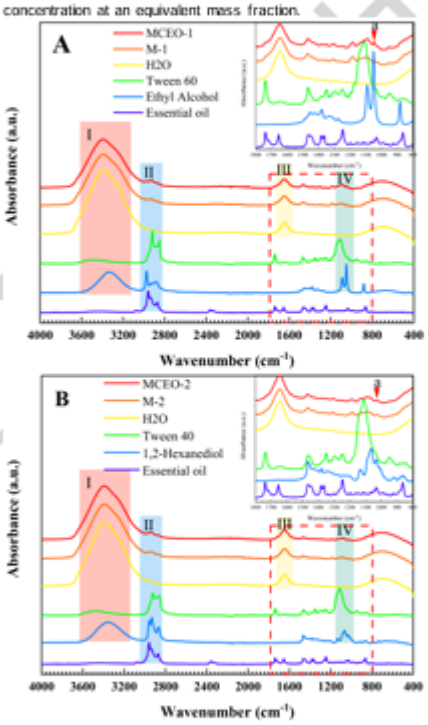

10.1002/cnma.202400554

RESEARCH ARTICLE

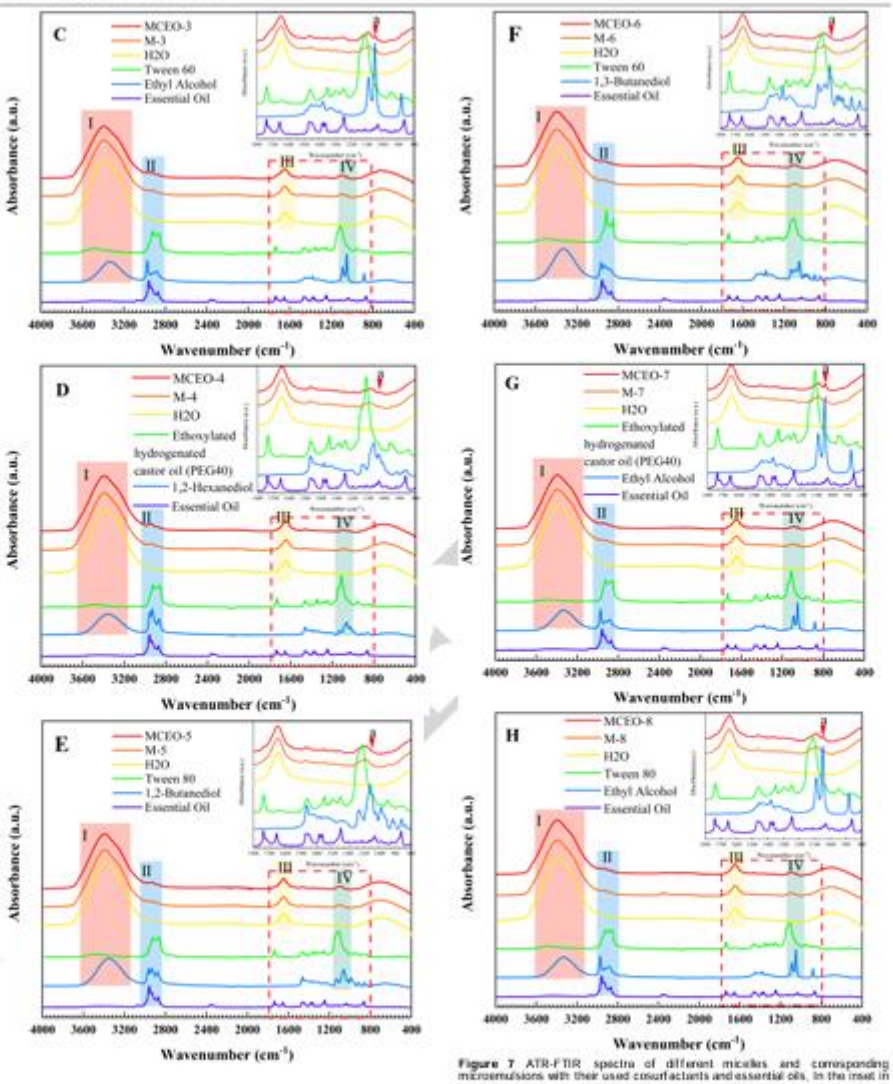

Figure 7 ATR-FTIR spectra of different micelles and corresponding microemulsions with their used cosurfactants and essential oils. In the inset in the upper right corner, point a corresponds to the infrared peak of the C-O bond of short-chain alcohol cosurfactants in the microemulsion (W/Mix-S = 0.2:0.8 from M-1 to M-8, O/W/Mix-S = 0.05:0.2:0.75 from MCEO-1 to MCEO-8) (Composition of the Mix-S-1 : Tween 80 (0.8, uL) & Ethyl Alcohol(0.2, uL); Mix-S-2 : Tween 40 (0.5, uL) & 1,2-Hexanediol (0.5, uL); Mix-S-3 : Tween 40 (0.75, uL) & Ethyl Alcohol (0.25, uL); Mix-S-4 : Ethoxylated hydrogenated castor oil (PEG40) (0.5, uL) & 1,2-Hexanediol (0.5, uL); Mix-S-5 : Tween 80 (0.8, uL) & 1,2-Butanediol (0.2, uL); Mix-S-6 : Tween 60 (0.67, uL) & 1,3-Butanediol (0.33, uL); Mix-S-7 : Ethoxylated hydrogenated castor oil (PEG40) (0.67, uL) & 1,2-Butanediol (0.33, uL); Mix-S-8 : Tween 80 (0.8, uL) & Ethyl Alcohol (0.2, uL).)

WILEY VCH

RESEARCH ARTICLE

3.3.3 Thermal stability of micelles and microemulsions

The thermal stability of micelles and microemulsions with various compositions was assessed via TGA experiments (Figure 9). Nonionic surfactants manifested pronounced temperature dependence, as the hydration of alkyl ethoxylate groups progressively diminished with increasing temperature, thereby altering their preferred curvature (Figure 8).

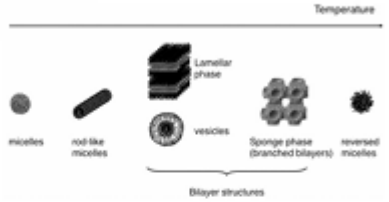

Figure 8 The effect of temperature on the micellar structure formed by nonionic surfactants.[33]

This relationship stems from the considerable variation in the solvation of the head groups of alkyl ethoxylates and alkylphenol ethoxylates with temperature, which in turn alters their geometrical requirements at the oil-water interface.[34] With rising temperature, the hydration of the essential oil head groups of alkyl ethoxylate surfactants decreased, thus requiring less space at the amphiphilic interface (Figure 10).[34] Consequently, at lower temperatures, these surfactants stabilized convex oil-water interfaces, while at higher temperatures, they stabilized concave oil-water interfaces (convex and concave are defined from the perspective of the aqueous phase). At intermediate temperatures, a flat interface was preferred. At a specific temperature, known as the phase inversion temperature, the mean curvature of the surfactant at the interface becomes ideally zero, resulting in a "balanced microemulsion." As the temperature increases, the microemulsion macroscopically transitions from an oil-in-water (O/W) structure to a bicontinuous phase and subsequently into a liquid crystalline phase or a water-in-oil (W/O) structure.[34]

By utilizing ω1, ω2, and ω3 alongside their corresponding temperatures, the thermal stability of various microemulsion systems was rigorously quantified (Figure 9). These parameters ideally correspond to the terminal temperatures of volatilization for water, cosurfactant, and essential oil, denoted as TA', TB', and TC', respectively. For systems incorporating volatile cosurfactants such as ethanol, as depicted in sections A, C, G, and H in Figure 8, the TGA curves of micelles and microemulsions demonstrated substantial overlap prior to reaching a certain temperature, indicative of congruent or highly analogous thermal behaviour at this juncture. This phenomenon is ostensibly attributable to the predominant volatilization of free water or the co-volatilization of water and ethanol. With further temperature escalation, the curvature of the amphiphilic interface layers within microemulsions and micelles undergoes alteration, precipitating the onset of essential oil volatilization.[35-37] Owing to the relatively sluggish volatilization rate of CEO, the TGA curves of microemulsions and micelles commence divergence. This divergence marks the inferred temperature at which essential oil volatilization initiates within the microemulsion. It is highly plausible that the essential oil co-volatilizes with water and ethanol, given the absence of distinct inflection points in the TGA curves of micelles and microemulsions at TB and TB', with such points only manifesting at TC and TC'.

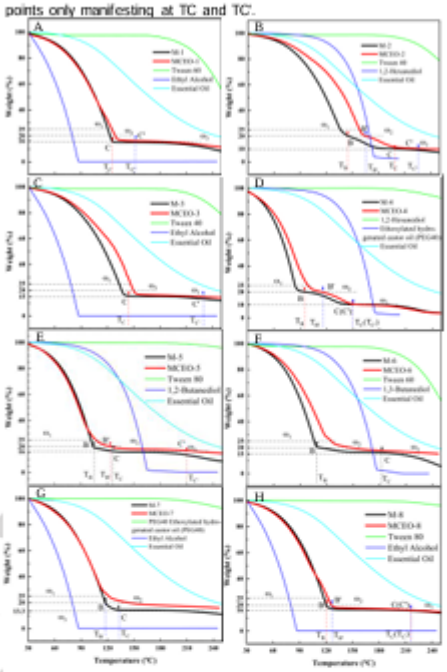

Figure 9 TGA results of different micelles and corresponding microemulsions (W/Mix-S = 0.2:0.8 from M-1 to M-8, O/W/Mix-S = 0.05:0.2:0.75 from MCEO-1 to MCEO-8) (Composition of the Mix-S-1 : Tween 60 (0.8, ω) & Ethyl Alcohol(0.2, ω); Mix-S-2 : Tween 40 (0.5, ω) & 1,2-Hexanediol (0.5, ω); Mix-S-3 : Tween 40 (0.75, ω) & Ethyl Alcohol (0.25, ω); Mix-S-4 : Ethoxylated hydrogenated castor oil (PEG40) (0.5, ω) & 1,2-Hexanediol (0.5, ω); Mix-S-5 : Tween 80 (0.8, ω) & 1,2-Butanediol (0.2, ω); Mix-S-6 : Tween 60 (0.67, ω) & 1,3-Butanediol (0.33, ω); Mix-S-7 : Ethoxylated hydrogenated castor oil (PEG40) (0.67, ω) & 1,2-Butanediol (0.33, ω); Mix-S-8 : Tween 80 (0.8, ω) & Ethyl Alcohol (0.2, ω).)

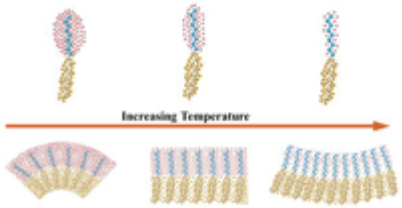

Figure 10 The effect of temperature variation on the curvature changes of the oil-water interface.

3.4 Antioxidant activity

In numerous prior investigations, limonene has been identified as a potent antioxidant capable of scavenging free radicals both in vivo and in vitro.[38-39] The radical scavenging capacities of various microemulsion systems incorporating CEO, as well as the pure essential oil, were meticulously assessed using the DPPH radical scavenging assay, PTIO radical scavenging assay, and hydroxyl radical scavenging assay were depicted in Figure 11.

Figure 11.A clearly demonstrated that the VE (vitamin E) equivalents for DPPH radical scavenging by MCEO were consistently superior to those of the pure essential oil. Notably, the microemulsion containing the surfactant Mix-S-6 exhibited the highest VE equivalent for DPPH radical scavenging, achieving 77.4 μg·mL^{-1}, nearly threefold higher than that of pure CEO (26.4 μg·mL^{-1}). This result was predominantly attributable to the solvent chemical environment of the essential oil. For substances with significant polarity, the incorporation of water can expedite hydrogen transfer during the free radical scavenging process.[40] In this experiment, methanol served as the solvent, and the antioxidant efficacy of CEO was markedly enhanced in the presence of water. This enhancement was also observable in the PTIO radical scavenging assay in Figure 11.B,[41] where the microemulsion with surfactant Mix-S-8 manifested the highest VC (vitamin C) equivalent for PTIO radical scavenging, measuring 297.5 μg·mL^{-1}, more than double that of pure CEO (129.2 μg·mL^{-1}).

However, as shown in Figure 11.C, in the hydroxyl radical scavenging assay, the scavenging rate of the essential oil (CEO) was consistently higher than that of the essential oil within the microemulsion. It is important to note that the scavenging rate of the essential oil in the microemulsion should be determined as the difference between the scavenging rate of the microemulsion (MCEO) and that of the microemulsion shell without essential oil (M). Additionally, the microemulsion shell without essential oil also exhibited a certain degree of radical scavenging ability, which was not observed in the DPPH and PTIO assays (Figure 11.A and Figure 11.B). This phenomenon may be attributed to the exceptionally high reactivity of hydroxyl radicals, which can react with surfactants even in the absence of essential oil. Therefore, for highly reactive radicals such as hydroxyl radicals, microemulsification may not effectively enhance the essential oil's radical-scavenging capability.

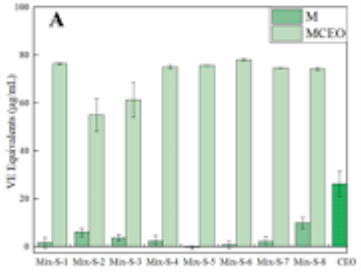

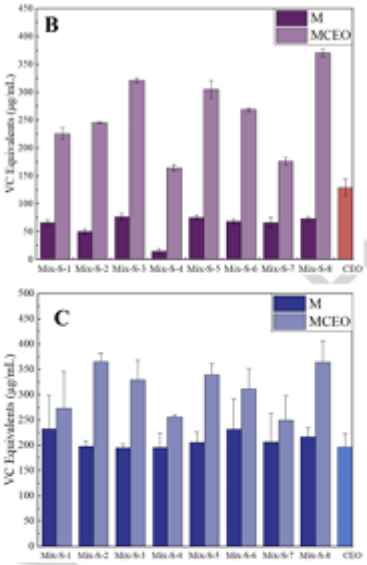

Figure 11 Antioxidant results of CEO, MCEO, and M assays with different free radicals (A: DPPH radical scavenging method, B: PTIO radical scavenging method, C: Hydroxyl radical scavenging method) (O/W/Mix-S = 0.05:0.2:0.75 from MCEO-1 to MCEO-8) (Composition of the Mix-S-1 : Tween 80 (0.8, wt) & Ethyl Alcohol(0.2, wt); Mix-S-2 : Tween 40 (0.5, wt) & 1,2-Hexanediol (0.5, wt); Mix-S-3 : Tween 40 (0.75, wt) & Ethyl Alcohol (0.25, wt); Mix-S-4 : Ethoxylated hydrogenated castor oil (PEG40) (0.5, wt) & 1,2-Hexanediol (0.5, wt); Mix-S-5 : Tween 80 (0.8, wt) & 1,2-Butanediol (0.2, wt); Mix-S-6 : Tween 60 (0.67, wt) & 1,3-Butanediol (0.33, wt); Mix-S-7 : Ethoxylated hydrogenated castor oil (PEG40) (0.67, wt) & 1,2-Butanediol (0.33, wt); Mix-S-8 : Tween 80 (0.8, wt) & Ethyl Alcohol (0.2, wt);)

4. Conclusion

This study systematically explores the quantitative relationship between the HLB values of polyoxyethylene nonionic surfactants and their mixtures with short-chain alcohols, focusing on the emulsification performance of microemulsions. Furthermore, it evaluates the physicochemical properties and in vitro antioxidant activity of microemulsions exhibiting optimal emulsification performance. The results of the pseudo-ternary phase diagrams reveal that microemulsions with HLB values ranging from 9.5 to 13.5 possess extensive single-phase emulsion regions (water content greater than 50%), while microemulsions with HLB values between 8.5 and 11.5 exhibit smaller biphasic regions. These results are comparable to existing findings, particularly in terms of HLB range. Hong et al. demonstrated that O/W emulsions formulated with Span and Tween surfactants achieved the smallest droplet size and higher zeta potential values within an HLB range of 10.7–10.8.[42] Similarly, Martin et al. studied thyme

WILEY-VCH

RESEARCH ARTICLE

essential oil emulsions and identified an optimal HLB range of 9–9.5 for stable formulations.[44]

The improvement in emulsification effectiveness is attributed to the presence of intermediate-chain-length co-surfactants such as 1,2-butanediol and 1,2-hexanediol, which reduce interfacial tension and favor higher entropy, leading to microemulsions with smaller particle sizes and higher dispersion.[44] This finding offers valuable guidance for surfactant selection in systems like drug delivery and personal care products, contributing to improved encapsulation efficiency, controlled release, and structural integrity.

SAXS studies further elucidate the relationship between phase structure transitions and water content (with a fixed oil ratio) during microemulsion preparation. Low water contents (below 0.2) cause distinctive interface between lipophilic phases and hydrophilic phases.[45] As water content increases, the distance between liquid crystalline layers expands, transitioning to a bicontinuous structure at 0.6 water content. With further increases in water content, the microemulsion structure evolves into ellipsoidal droplets, with symmetry improving as water content continues to rise, ultimately forming perfectly symmetric spherical droplets. Characterization of the physicochemical properties of the microemulsions reveals a stable pH range (3.5-6.5) and particle sizes (15 nm-35 nm). The addition of essential oils leads to micelle expansion, resulting in larger microemulsion droplets, increased PDI, and decreased absolute zeta potential values. This indicates that environmental conditions, such as the use of Tween 60 (pH = 3.5), should be considered when selecting surfactants. ATR-FTIR confirms the formation of O/W micelles, with co-surfactants potentially located at the micelle interface. The incorporation of high-boiling, low-volatility medium-chain alcohols as co-surfactants can significantly enhance the thermal stability of microemulsions, thermally stable microemulsions can act as safe carriers for flavors, natural pigments in food, or as perfume alternatives, preventing volatilization during storage and transport. Water-based systems also enhance safety.

In vitro antioxidant tests revealed that microemulsification enhances the reactivity of essential oils toward DPPH and PTIO radicals by accelerating hydrogen transfer in the presence of water, indicating improved antioxidant performance. This conclusion highlights that microemulsification can protect vitamin E (VE), improve its water solubility, and enhance its antioxidant capacity, thereby boosting the efficacy of VE in functional foods and cosmetics.

Acknowledgements

This work was supported by the National Thousand Young Talents Program of China.

Keywords: Microemulsion, Thermal stability, Phase structure transformation, *Juniperus chinensis Roxb.*

[1] Stanislaw Slomkowski, José V. Alemán, Robert G. Gilbert, Michael Hess, Kazuyuki Horie, Richard G. Jones, Przemyslaw Kubisa, Ingrid Meisel, Werner Mormann, Stanislaw Penczek, R. F. T. Stepto, *Pure Appl. Chem* **2011**, *83*, 2229-2259.
[2] T. P. Hoar, J. H. Schulman, *NATURE* **1943**, *152*, 102-103.
[3] A. Froelich, T. Osmałek, A. Snela, P. Kunstman, B. Jadach, M. Olejniczak, G. Roszak, W. Bielas, *J. Colloid Interface Sci.* **2017**, *507*, 323-336.
[4] C. Shen, J. Li, Q. Meng, L. Xu, G. Zhang, *Food Chem* **2024**, *457*, 140167-140167.
[5] M. Ghorbanzadeh, N. Farhadian, S. Golmohammadzadeh, M. Karimi, M. Ebrahimi, *Colloids Surf., B* **2019**, *179*, 393-404.
[6] M. Bourrel, C. Chambu, R. S. Schechter, W. H. Wade, *Society of Petroleum Engineers Journal* **1982**, *22*, 28-36.
[7] H. S. Linda Ström*, Per-Anders Carlsson, Magnus Skoglundh, and Hanna Härelind, *Langmuir* **2018**, *34*, 9754-9761.
[8] ISSA LO, ALEXANDER T. FLORENCE, JEAN-PAUL TREGUIER, MONIQUE SEILLER, F. PUISIEUX, *J. Colloid Interface Sci.* **1976**, *59*.
[9] Q. Wang, H. Zhang, Y. Han, Y. Cui, X. Han, *RSC Adv.* **2023**, *13*, 24692-24698.
[10] A. Pant, K. Jha, M. Singh, *IOSR Journal of Pharmacy and Biological Sciences(IOSR-JPBS)* **2019**, *14*, 1-6.
[11] D. J. Miller, T. Henning, *TENSIDE SURFACTANTS DETERGENTS* **2005**, *42*, 34-39.
[12] W. C. Griffin, *Journal of the Society of Cosmetic Chemists 1* **1949**, 311-326.
[13] A. GUINIER, *SMALL-ANGLE SCATTERING OF X-RAYS* **1955**.
[14] G. Panick, R. Malessa, R. Winter, G. Rapp, K. J. Frye, C. A. Royer, *J. Mol. Biol.* **1998**, *275*, 389-402.
[15] Porod G. Kolloid-Z, *Kolloid-Zeitschrift* **1951**, *124*, 83–114.
[16] Z.-H. Li, *Chin. Phys. C* **2013**, *37*.
[17] H. D. Bale, P. W. Schmidt, *Phys. Rev. Lett.* **1984**, *53*, 596-599.
[18] Y. Asnes, A. Hymete, H. Admassu, A. Ayalew, *Int. J. Food Prop.* **2024**, *27*, 549-565.
[19] X. Li, *J. Agric. Food. Chem* **2017**, *65*, 6288-6297.
[20] M. Li, X. Zhao, M. Xu, in *Foods*, *Vol. 11*, **2022**.
[21] M. Gradzielski, M. Duvail, P. Maio de Molina, M. Simon, Y. Talmon, T. Zemb, *Chem Rev.* **2021**, *121*, 5671-5740.
[22] E. Ruckenstein, *Chem Phys Lett.* **1978**, *57*, 517-521.
[23] J. N. Israelachvili, D. J. Mitchell, B. W. Ninham, *Journal of the Chemical Society-Faraday Transactions II* **1976**, *72*, 1525-1568.
[24] M. Gradzielski, H. Hoffmann, D. Langevin, *J. Phys. Chem* **1995**, *99*, 12612-12623.
[25] P. Juthaporn, L. Sontaya, L. Chutima, *Foods* **2024**, *13*, 2570-2570.
[26] J. Ponphaiboon, S. Limmatvapirat, C. Limmatvapirat, *MOLECULES* **2024**, *29*.
[27] H. N. W. Lekkerkerker, W. K. Kegel, J. T. G. Overbeek, *Berichte der Bunsengesellschaft für physikalische Chemie* **2010**, *100*, 206-217.
[28] Q. Liu, J. Wang, H. Wu, S. Zong, N. Wang, T. Wang, L. Zhou, X. Huang, H. Hao, *J. Mol. Liq.* **2022**, *349*, 118425.
[29] A. Kogan, D. E. Shalev, U. Ronin, A. Aserin, N. Garti, *The Journal of Physical Chemistry B* **2009**, *113*, 10669-10678.
[30] O. Regev, S. Ezrahi, A. Aserin, N. Garti, E. Wachtel, E. W. Kaler, A. Khan, Y. Talmon, *Langmuir* **1996**, *12*, 668-674.
[31] Z. H. Li, J. H. Sun, J. P. Zhao, D. Wu, Y. H. Sun, Y. Liu, W. J. Sheng, B. Z. Dong, *Acta Physica Sinica* **2000**, *49*, 775-780.
[32] J.-P. Hsu, A. Nacu, *J. Colloid Interface Sci.* **2003**, *259*, 374-381.
[33] B. Lindman, B. Medronho, G. Karlström, *Current Opinion in Colloid & Interface Science* **2016**, *22*, 23-29.
[34] K. Shinoda, H. Arai, *J. Phys. Chem* **1964**, *68*, 3485-&.
[35] M. Gradzielski, M. Duvail, P. M. de Molina, M. Simon, Y. Talmon, T. Zemb, *Chem Rev.* **2021**, *121*, 5671-5740.
[36] G. Tartaro, H. Mateos, D. Schirone, R. Angelico, G. Palazzo, *Nanomaterials* **2020**, *10*.
[37] T. Shikata, M. Okuzono, N. Sugimoto, *Macromolecules* **2013**, *46*, 1956-1961.
[38] S. Malhotra, S. Suri, R. Tuli, *Planta Med.* **2009**, *75*, 62-64.
[39] A. A. C. de Almeida, R. B. F. de Carvalho, O. A. Silva, D. P. de Sousa, R. M. de Freitas, *Pharmacology Biochemistry and Behavior* **2014**, *118*, 69-78.
[40] I. Gulcin, S. H. Alwasel, *Processes* **2023**, *11*.
[41] X. Li, *J. Agric. Food. Chem* **2017**, *65*, 6288-6297.
[42] I. K. Hong, S. I. Kim, S. B. Lee, *J. Ind. Eng. Chem* **2018**, *67*, 123-131.
[43] M. José Martín, L. A. Trujillo, M. Carmen García, M. Carmen Alfaro, J. Muñoz, *J. Dispersion Sci. Technol.* **2018**, *39*, 1627-1634.
[44] A. E. Edris, C. F. R. Malone, *Int. J. Cosmet. Sci.* **2012**, *34*, 441-450.
[45] W. Dongqi, Y. Daiyin, W. Junda, Z. Yaohou, Z. Chengli, *J. Pet. Explor. Prod. Technol.* **2022**, *12*, 2735-2746.

https://doi.org/10.1002/cnma.202400554

CHEMNANOMAT

CHEMISTRY OF NANOMATERIALS FOR ENERGY, BIOLOGY AND MORE

www.chemnanomat.org

Accepted Article

Title: The Elucidation of the Critical Role of HLB value in Microemulsions Formulation

Authors: Mingjun Tang, Min Ling, Wenjing Ma, Wenqian Sheng, and Wenjun Yan

To be cited as: *ChemNanoMat* **2025**, e202400554

Link to VoR: https://doi.org/10.1002/cnma.202400554

A Journal of

ACES Asian Chemical Editorial Society

WILEY VCH